A Frequency-Adaptive Delay Signal Cancelation Based Filter to Reduce Position Estimation Error for Sensorless IPMSM Drives

Zheng Wu, Chenwen Cheng, Wei Hua, *Senior Member, IEEE*, Yuchen Wang, Hengliang Zhang,
and Wei Wang, *Senior Member, IEEE*

***Abstract*—In a sliding mode observer-based sensorless drive system, the estimated back electromotive force (BEMF) always contains abundant low-order harmonics caused by nonideal factors, e.g., flux spatial harmonics, inverter nonlinearity, and current measurement error, resulting in large estimated position errors. In previous studies, adaptive notch filters are usually adopted to suppress the BEMF harmonics. However, these filters suffer from enormous computation and increase system complexity, especially facing numerous low-order harmonics. In this article, a new frequency-adaptive notch filter employing delay signal cancelation (DSC) is proposed, which can be tailored to eliminate multiple harmonics with a simple structure. First, Lagrange interpolation is applied to realize fractional-order delay in the frequency-adaptive DSC (FADSC). Then, a frequency-dividing record method is designed to shorten the recording array length for the FADSC at low speed. Next, a switching procedure is introduced to change the frequency-dividing factor smoothly at different speeds. Finally, the transformation matrix in the DSC is changed in the FADSC by adding the rotation direction to make it suitable to forward and reverse rotations of an interior permanent magnet synchronous machine (IPMSM). The accuracy of the estimated rotor position can be improved by FADSC, which is verified by experiments on a prototype IPMSM.**

***Index Terms*—Frequency-adaptive delay signal cancelation (FADSC), interior permanent magnet synchronous machine (IPMSM), sensorless control, sliding mode observer (SMO).**

I. INTRODUCTION

INTERIOR permanent magnet synchronous machine (IPMSM) has been widely used in modern industry because of their high efficiency and high power density [1]. In an IPMSM-based drive, the accurate rotor position is vital for speed-closed loop control, which can be measured by physical sensors, such as encoders [2], resolvers [3], and hall sensors [4]. However, these sensors not only increase the cost of the control system but also weaken the system's reliability in harsh environments [5]. Alternative sensorless control strategies have been widely studied to overcome these drawbacks of physical sensors.

Generally, the sensorless strategies can be roughly divided into two categories: saliency-based and back electromotive force (BEMF)-based methods [6], where the former is normally applied at zero/low speeds, and the latter is suitable at medium/high speeds. The concept of BEMF-based methods is to estimate the BEMF by employing observers, including sliding mode observer (SMO) [7], extended Kalman filter [8], state observer [9], disturbance observer [10], and model reference adaptive system [11]. Among them, the SMO method is extensively adopted due to its simple structure, good dynamic performance, and robustness to parameter variations [12].

In an SMO, the BEMF is obtained from the difference between estimated and measured phase currents. Hence, the estimated BEMF is sensitive to phase current harmonics, which are affected by flux spatial harmonics and the inverter nonlinearity [13], [14], [15], [16], [17], [18], [19], [20], [21], [22], [23], [24], [25]. Both the flux spatial harmonics and the inverter nonlinearity will result in the $6k\pm1$ order phase current harmonics, which are transferred into the estimated BEMF harmonics in SMO. Moreover, the phase current measurement error from the sampling circuit is inevitable even if it is well designed due to the following factors, such as the nonlinearity of Hall current sensors, the thermal drift of analog elements, and the nonlinearity of A/D converters [13], [14], [15] Furthermore, the current measurement error will produce low-order harmonics in the estimated BEMF, which unfavorably lead to inaccurate rotor positions, increased torque ripples and power losses.

To reduce the position estimation error, many methods based on the BEMF-harmonic suppression principle have been proposed [16], [17], [18], [19], [20], [21], [22], [23], [24], [25]. However, in [16], [17], and [18] only the inverter nonlinearity is compensated, but the flux spatial harmonics and current measurement errors are not considered. The resonant filters proposed in [19], [20], and [21] can extract the fundamental component from the estimated BEM, but their low-order-harmonic

---

Manuscript received 30 June 2022; accepted 9 October 2022. Date of publication 13 October 2022; date of current version 18 November 2022. This work was supported in part by the National Key Research and Development Program under (2021YFB2500701), in part by the National Natural Science Foundation of China under Grant 51825701, and in part by the Key R&D Program of Jiangsu Province under Grant BE2022053-2. Recommended for publication by Associate Editor U. Deshpande. *(Corresponding author: Wei Hua.)*

The authors are with the School of Electrical Engineering, Southeast University, Nanjing 210096, China (e-mail: wuzheng96@seu.edu.cn; chenwen_cheng@seu.edu.cn; huawei1978@seu.edu.cn; wangyuchen1994@seu.edu.cn; zhanghengliang@seu.edu.cn; wangwei1986@seu.edu.cn).

Color versions of one or more figures in this article are available at https://doi.org/10.1109/TPEL.2022.3214270.

Digital Object Identifier 10.1109/TPEL.2022.3214270

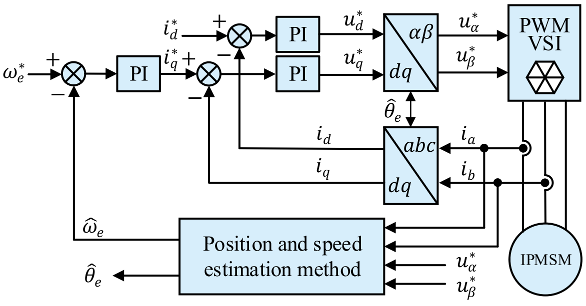

Fig. 1. Block diagram of a sensorless drive system for an IPMSM.

suppression effects are still unsatisfactory. In [22], [23], [24], and [25], adaptive notch filters based on the algorithms, including least-mean-squares, recursive-least-square, bilinear recursive-least-square or adaptive linear neural network, are introduced to eliminate the specific harmonics, respectively, however, where many coefficients need to be tuned online and the complexity of estimation system is increased, especially when eliminating abundant low-order harmonics.

Different from the adaptive notch filters introduced above, the delay signal cancelation (DSC) needs no online tuned coefficients and can eliminate a series of harmonics with a simple structure [26], [27]. It is normally used in a power grid with a fixed fundamental frequency of 50/60 Hz, which means that the conventional DSC is not suitable for a varying-frequency scenario.

In this article, a new adaptive filter based on frequency-adaptive DSC (FADSC) is proposed to eliminate the estimated BEMF harmonics in SMO for the adjustable-speed motor drive. First, Lagrange interpolation is applied to approximate the fractional order delay in FADSC. Second, a frequency-dividing record method is designed to apply FADSC at lower frequencies under the limitation of the record array length. Third, a switching procedure is implemented for FADSC to change different frequency-dividing factors smoothly. Finally, a transformation matrix with the rotation direction information is adopted to make FADSC work in both forward and reverse rotations of the motor.

The organization of this article is as followed. In Section II, the SMO structure is introduced, where the effects of inverter nonlinearity, flux spatial harmonics, and current measurement errors on the estimated BEMF harmonics are analyzed. Then, the structure and design principle of the proposed FADSC are introduced in Section III. Then, in Section IV a series of experiments are carried out to verify the effectiveness of the proposed FADSC. Finally, Section V concludes this article.

II. SMO-BASED IPMSM SENSORLESS DRIVE SYSTEM

An IPMSM sensorless drive system is shown in Fig. 1. The position and speed estimation method is based on an SMO with a phase-locked loop (PLL) as shown in Fig. 2. In the following, the structure of the SMO is introduced first. Then, the impacts of common nonideal factors on the estimated BEMF are analyzed.

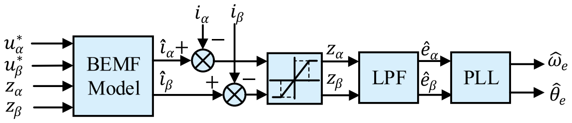

Fig. 2. Structure of the SMO-based position and speed estimation method.

A. SMO-Based Sensorless Control Method

The BEMF model of an IPMSM in $\alpha\beta$-axes is expressed as

$$\begin{bmatrix} u_\alpha \\ u_\beta \end{bmatrix} = \begin{bmatrix} R_s + pL_d & \omega_e (L_d - L_q) \\ -\omega_e (L_d - L_q) & R_s + pL_d \end{bmatrix} \begin{bmatrix} i_\alpha \\ i_\beta \end{bmatrix} + \begin{bmatrix} e_\alpha \\ e_\beta \end{bmatrix} \tag{1}$$

where u_α/u_β and i_α/i_β are $\alpha\beta$-axes stator voltages and currents, L_d/L_q are dq-axes inductances, R_s is phase winding resistance, ω_e is electrical angular speed, and p is the differential operator.

Besides, e_α/e_β are BEMFs in the stationary $\alpha\beta$ frame as

$$\begin{bmatrix} e_\alpha \\ e_\beta \end{bmatrix} = \left((L_d - L_q)(\omega_e i_d - p i_q) + \omega_e \varphi_f \right) \begin{bmatrix} -\sin\theta_e \\ \cos\theta_e \end{bmatrix} \tag{2}$$

where i_d/i_q are stator currents in the rotating dq frame, θ_e is the rotor electrical angle, and φ_f is PM flux-linkage.

The current differential function is expressed in the following equation based on (1), where the $\alpha\beta$-axes BEMFs are represented by the estimated $\alpha\beta$-axes BEMFs (z_α/z_β):

$$\begin{aligned} p \begin{bmatrix} \hat{\imath}_\alpha \\ \hat{\imath}_\beta \end{bmatrix} = {} & p \frac{1}{L_d} \begin{bmatrix} -R_s & \hat{\omega}_e (L_d - L_q) \\ -\hat{\omega}_e (L_d - L_q) & -R_s \end{bmatrix} \begin{bmatrix} \hat{\imath}_\alpha \\ \hat{\imath}_\beta \end{bmatrix} \\ & + \frac{1}{L_d} \left(\begin{bmatrix} u_\alpha \\ u_\beta \end{bmatrix} - \begin{bmatrix} z_\alpha \\ z_\beta \end{bmatrix} \right) \end{aligned} \tag{3}$$

where ˆ represents the measured values, and z_α/z_β are obtained from the difference between the estimated and measured currents by a saturation function as

$$\begin{bmatrix} z_\alpha \\ z_\beta \end{bmatrix} = k_s \begin{bmatrix} \text{sat}\left(\hat{\imath}_\alpha - i_\alpha\right) \\ \text{sat}\left(\hat{\imath}_\beta - i_\beta\right) \end{bmatrix} \tag{4}$$

where k_s is the sliding mode gain, which is larger than $(e_\alpha, e_\beta)_{\max}$, and sat() is the saturation function.

In Fig. 2, a low-pass filter (LPF) is applied to suppress the high-frequency noise in the z_α/z_β. Thus, the estimated BEMFs are further expressed as

$$\begin{bmatrix} \hat{e}_\alpha \\ \hat{e}_\beta \end{bmatrix} = \begin{bmatrix} \text{LPF}(z_\alpha) \\ \text{LPF}(z_\beta) \end{bmatrix}. \tag{5}$$

The estimated BEMFs are then inputted into a PLL to estimate the rotor position and speed, as illustrated in Fig. 2.

B. BEMF Harmonics Caused By Nonideal Factors

The LPF in SMO can only filter out the high-frequency harmonics in the estimated BEMF. But the estimated BEMF also contains abundant low-order harmonics, caused by the flux spatial harmonics, inverter nonlinear, and current measurement error, which result in position estimated errors, and need to be removed by an extra filter. In the following, the specific orders of these low-order harmonics are analyzed.

TABLE I
EFFECT OF NONIDEAL FACTORS ON BEMF HARMONICS

Factors	Harmonic order
Flux spatial harmonics and Inverter nonlinearity	–5 and +7
Offset current measurement error	0 and +2
Scaling current measurement error	–1 and +3

The flux spatial harmonics and inverter nonlinearity will generate the $6k\pm1$ order harmonics in stator currents, and consequently the $6k\pm1$ order harmonics in the estimated BEMF [22], [23], [24], [25]. Hence, only the effects of 5-order negative sequence and 7-order positive sequence harmonics are emphasized considering the amplitude of these harmonics.

As another nonideal factor, the current measurement error is analyzed considering the nonlinearity of Hall sensors, the thermal drift of analog elements, and the nonlinearity of A/D converters. The current measurement error consists of the offset error and scaling error, which can be expressed in the phase current error as

$$\begin{cases} \Delta\, i_a = s_a\, I_1 \cos(\omega_e t) + o_a \\ \Delta\, i_b = s_b\, I_1 \cos(\omega_e t - 2\pi/3) + o_b \\ \Delta\, i_c = \ -\Delta i_a - \Delta i_b \end{cases} \tag{6}$$

where s_a/s_b and o_a/o_b are the scaling and offset currents errors of phases A and B, and I_1 is the amplitude of phase current.

The BEMF harmonics affected by the current measurement error are obtained by transforming (6) into the rotating *dq* frame and then substituted into (2) as

$$\begin{cases} \Delta\, e_\alpha = H_1\, H_2 \cos(2\omega_e t + \mu_1) - H_1 H_2 \cos\mu_1 \\ \quad +1.5 H_1 H_3 \cos(3\omega_e t + \pi/3) + H_1 H_4 \sin(-\omega_e t) \\ \quad -1.5 H_1 H_3 \cos(-\omega_e t - \pi/3) \\ \Delta\, e_\beta = H_1\, H_2 \sin(2\omega_e t + \mu_1) + H_1 H_2 \sin\mu_1 \\ \quad +1.5 H_1 H_3 \sin(3\omega_e t + \pi/3) + H_1 H_4 \cos(-\omega_e t) \\ \quad -1.5 H_1 H_3 \sin(-\omega_e t - \pi/3) \end{cases} \tag{7}$$

where

$$H_1 = (L_d - L_q)\ \omega_e,\ \ H_2 = 2\sqrt{(o_a^2 + o_a o_b + o_b^2)/3},$$

$$H_3 = I_1\ (s_a - s_b)/\sqrt{3},\ \ H_4 = I_1\ (s_a + s_b)/2,$$

$$\mu_1 = \tan^{-1}\left(\sqrt{3} o_a/(o_a + 2 o_b)\right).$$

It can be observed from (7) that the current measurement errors produce abundant low-order harmonics in the estimated BEMF. Among them, the 0-order (dc-biased) and 2-order positive sequence harmonics are related to the offset error, whereas the 3-order positive sequence components and 1-order negative sequence components are caused by the scaling error.

The main harmonics caused by flux spatial harmonics, inverter nonlinearity, and current measurement errors are listed in Table I.

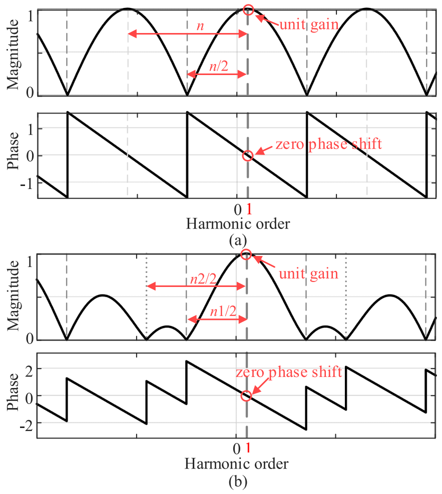

Fig. 3. Bode diagram of DSC. (a) DSC_n. (b) Cascade of DSC_{n1} and DSC_{n2}.

III. STRUCTURE AND DESIGN OF FADSC

A. Conventional DSC

The estimated BEMF harmonics feature periodicity, is utilized by DSC to eliminate a series of harmonics with specific orders. The transfer function of the conventional DSC is expressed as

$$G_{\mathrm{DSC}}\ (s) = \frac{1 + e^{j\frac{2\pi}{n} - \frac{2\pi}{n\omega_0}s}}{2} \tag{8}$$

where n is the delay factor and ω_0 is the fundamental angular frequency.

Based on the transfer function, the bode diagram of DSC is presented in Fig. 3. It can be observed from Fig. 3 that the DSC has unit gain and zero phase shift at first-order harmonic, and zero gain at a series of the harmonics, which are determined by the n and expressed as follows:

$$N_{eli} = 1 + \frac{bn}{2},\ b = \pm1, \pm2, \pm3 \ldots \tag{9}$$

where N_{eli} represents the orders of eliminating harmonics.

To be implemented on a digital processor, the DSC should be expressed in its discretization form. The discretized DSC can be deduced when applying it to eliminate the $\alpha\beta$-axes estimated BEMF harmonics as

$$\mathrm{DSC}_n\ (\boldsymbol{e_s}[k_t]) = \frac{1}{2}\,\boldsymbol{e_s}[k_t]\left(1 + \boldsymbol{R}\left(\frac{2\pi}{n}\right) z^{-D}\right) \tag{10}$$

where k_t is the sampling point, $\boldsymbol{e_s}$ represents the $\alpha\beta$-axes signal matrix ($[e_\alpha,\ e_\beta]^{\mathrm{T}}$), and the transformation matrix $\boldsymbol{R}()$ and the delay number D is given in the following equations:

$$\boldsymbol{R}(\theta) = \begin{bmatrix} \cos\theta & -\sin\theta \\ \sin\theta & \cos\theta \end{bmatrix} \tag{11}$$

$$D = \frac{2\pi f_s}{n\omega_0} \tag{12}$$

where f_s is the sampling frequency.

A single DSC can eliminate a series of harmonics, but it cannot eliminate the harmonics not satisfied with (9). Thus, a cascade of multiple DSCs is generally adopted for the abundant harmonics and its transfer function is expressed as

$$G_{\mathrm{CDSC}}\ (s) = \prod_{k=1}^{K} \frac{1 + e^{j\frac{2\pi}{n_k} - \frac{2\pi}{n_k \omega_0} s}}{2} \tag{13}$$

where K is the number of DSC in cascade.

The bode diagram of the cascade of DSC$_{n1}$ and DSC$_{n2}$ is presented in Fig. 3(b), where the unit gain and zero phase shift at first-order harmonic remain. Besides, the eliminated harmonic orders of cascaded DSC consisted of those of DSC$_{n1}$ and DSC$_{n2}$, which indicates each DSC in cascade can be analyzed independently to reveal characteristics of the cascaded DSC. Thus, the following modifications carried out on the single DSC are reasonable.

B. Fractional Delay (FD) for FADSC

In a fixed-frequency system, T_s can be specially designed to guarantee that D is an integer. However, ω_0 should be set as the rotor electrical angular position in a variable-frequency drive system, which means D might be noninteger. If D is fractional, the time delay item cannot be obtained directly. To solve this problem, Lagrange interpolation is adopted.

First, the time delay number (D) is divided into the integer part (D_n) and the fractional part (D_f) as

$$D_n = \text{floor}\,(D)\,, \quad D_f = D - D_n \tag{14}$$

where floor(D) is the function to obtain the maximum integer less than D.

Then, the FD is approximated by Lagrange interpolation in the discrete domain as

$$\mathrm{FD}\ \left(z^{-D}\right) = \sum_{a=0}^{N} L_a z^{-D_n - a} \tag{15}$$

where N is the order of Lagrange interpolation, and the interpolation coefficient L_a is given as

$$L_a = \prod_{\substack{i=0 \\ i \neq a}}^{N} \frac{D_f - i}{a - i}\,. \tag{16}$$

For Lagrange interpolation-based FD (LI-FD), the order (N) is the only coefficient to design. From (15) and (16), the numbers of multiplication and addition are ($2N^2 + 2N$) and ($2N^2 + 3N$), respectively, in the N-order LI-FD. Obviously, the resultant computation of LI-FD increases geometrically with N. Considering the processor's computation capacity, the high order ($N > 3$) LI-FD is not considered in this article. To further determine the LI-FD order, Fig. 4 gives magnitude response of the LI-FD for $N = 1$, 2, and 3 in the worst-case approximation ($D = 0.5$) [28]. In Fig. 4, the low-order LI-FD can obtain good approximations at low normalized frequency. Besides, the magnitude response of the 2-order LI-FD (dashed line) is closer to the unit magnitude than that of the 1-order LI-FD (solid line) in the whole normalized frequency range. Moreover, the magnitude of the 3-order LI-FD (dotted line) exceeds the unit magnitude, which might lead to a stability problem. Accordingly, the 2-order LI-FD is recommended.

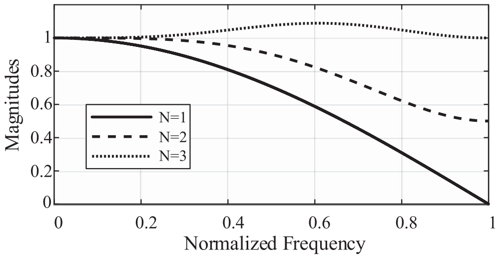

Fig. 4. Magnitude response of the FD based on Lagrange interpolation for $D = 0.5$ and $N = 1$, 2, and 3. Normalized frequency is defined as $2f_{\mathrm{h}}/f_s$, where f_{h} is the harmonic frequency.

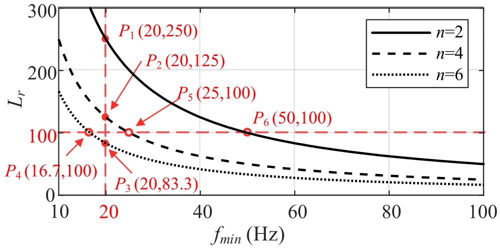

Fig. 5. Relationship between record array length (L_r) and minimum application frequency ($f_{\min}$) of FADSC for $f_s = 10$ kHz and the delay factor $n = 2$, 4, and 6.

For the 2-order LI-FD, its magnitudes decrease versus the increase of normalized frequency, which is defined as the ratio of the objective harmonic frequency to half of the sampling frequency (f_s). In the estimated BEMF, the 7-order harmonic has a maximum frequency of 933.3 Hz at the rated angular frequency (133.3 Hz) of the prototyped IPMSM. This rated 7-order harmonic frequency corresponds to a magnitude response is 0.9974 in the case of $f_s = 10$ kHz, demonstrating the effectiveness of the 2-order LI-FD.

C. Frequency-Dividing Record Method for FADSC

In a digital system, the data record is the premise of realizing time delay, and it needs a long enough array. The long length of the array can be caused by low fundamental frequency, occupying high memory consumption, under the fixed sampling frequency condition. Nevertheless, the memory of a digital processor is an important and restricted resource, especially in a complex control system, which limits the length of the record array.

The record array length (L_r) is related to the minimum frequency ($f_{\min}$) of the input signal to realize the time delay and their relationship yields

$$L_r = \frac{f_s}{n f_{\min}}. \tag{17}$$

As shown in (17), the record array length is also affected by the delay factor (n) and sampling frequency (T_s), apart from $f_{\min}$. The effects of n and $f_{\min}$ on L_r are illustrated in Fig. 5 in the case of a 10 kHz sampling frequency. Fig. 5 reveals that

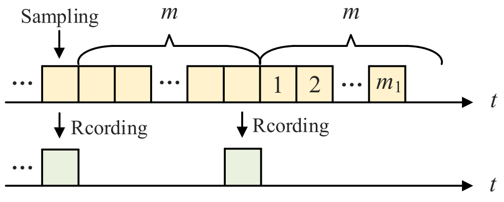

Fig. 6. Instruction of the frequency-dividing record method.

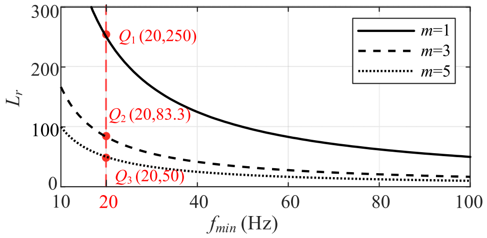

Fig. 7. Effect of the frequency-diving factor (m) on the recording array length (L_r) and minimum frequency ($f_{\min}$) for FADSC with $n = 2$ in the cases of $m =$ 1, 3 and 5.

the record array length is reversely proportional to the minimum frequency and the delay factor.

The lowest frequency of SMO is set as 20 Hz considering the signal-to-noise ratio of the estimated BEMF of the prototyped motor. Accordingly, the record array lengths at $f_{\min} = 20$ Hz for $n = 2$, 4, and 6 are marked as P_1, P_2, and P_3 in Fig. 5. The record array needs to record 250 floating-point data for realizing time delay at $n = 2$. The record array length will come to 500 and consume lots of memory if a 2-order FADSC is used to eliminate the harmonics in the $\alpha\beta$-axes BEMFs. The other two record arrays at $n = 4$ and 6 suffer similar problems, even though their lengths are shorter than that at $n = 2$. On the other hand, if the maximum length of the recording array is limited to 100, FADSC will fail to work at 20 Hz for $n = 2$ and 4, shown as P_5 and P_6 in Fig. 5, respectively. Moreover, the application of cascaded FADSC will increase memory consumption further, which is not allowed.

To solve this problem, a frequency-dividing record method is proposed. It can make the array record the BEMF data every m sampling period as shown in Fig. 6. The FADSC is rewritten based on this method as

$$\mathrm{FADSC}_{\mathrm{n(m)}}\ (\boldsymbol{e_s}\,[k_t]) = \frac{1}{2}\,\boldsymbol{e_s}\,[k_t]\left(1+\boldsymbol{R}\left(\frac{2\pi}{n}\right)z^{-D_m}\right) \tag{18}$$

where D_m is a new delay number and expressed as

$$D_m = \frac{2\pi f_s}{nm\omega_0} - \frac{m_1}{m} \tag{19}$$

where m_1 is the counter of frequency dividing shown in Fig. 6.

Using the dividing-frequency recording method, the relationship between the record array length and minimum frequency becomes

$$f_{\min} = \frac{f_s}{nmL_r}. \tag{20}$$

The impact of frequency-dividing factor (m) on $f_{\min}$ and L_r for $n = 2$ is illustrated in Fig. 7, which demonstrates that L_r is proportion to m for a specific $f_{\min}$. $m = 3$ and 5 can decrease L_r of an FADSC with $n = 2$ by 166.7 and 200, respectively, which is a significant improvement.

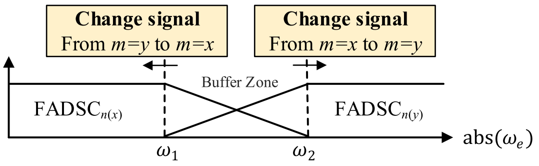

Fig. 8. Arrangement of $\mathrm{FADSC}_{n(m)}$ with different frequency-dividing factors.

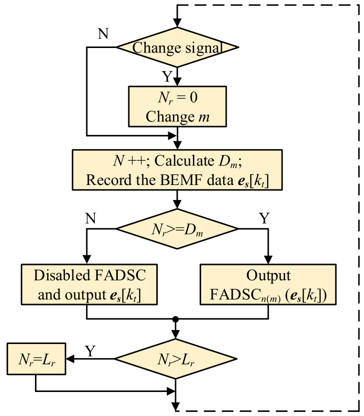

Fig. 9. Flowchart for the frequency-dividing factor changing procedure.

D. FADSC Frequency-Dividing Factor Change Method

The above frequency-dividing record method is to decrease the sampling frequency from f_s to f_s/m for an LI-FD, and it increases the normalized frequency equivalently. Consequently, the approximation of an LI-FD with a large frequency-dividing factor becomes unsatisfactory at the high speed as shown in Fig. 4. For example, the magnitude response of the 5-order harmonic decreases from 0.9993 to 0.9542 when m changes from 1 to 3 at rated speed (133.3 Hz). Its corresponding magnitude becomes 0.7605 for $m = 5$. Hence, the frequency-dividing factor should be changed at different motor speeds to overcome this drawback.

Hence, an arrangement of FADSC with different frequency-dividing factors is illustrated in Fig. 8. To avoid frequent switching, the changing moments of m corresponding to speed-down and speed-up are separated and set at ω_1 and ω_2, respectively. For a good approximation of LI-FD, ω_1 is set as the minimum frequency of 2-order LI-FD with $m = y$, and ω_2 is suggested as the value not to decrease the magnitude response of the 2-order LI-FD heavily.

A changing procedure is designed to make the frequency-dividing factor change smoothly as presented in Fig. 9. Its key concept is to disable FADSC until the number of record data under the new frequency-dividing factor is larger than the delay number. The dashed line in Fig. 9 represents the other procedures necessary for a sensorless IPMSM control system.

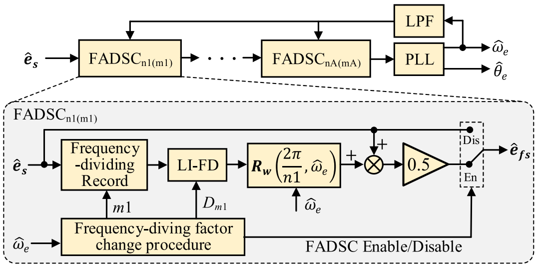

Fig. 10. Whole block diagram of the proposed FADSC.

TABLE II
IMPLEMENTATION OF THE FADSC$_{n(m)}$

BEMF harmonic orders	FADSC$_{n(m)}$	Change signal frequency
0 and +2	FADSC$_{2(1)}$ or FADSC$_{2(5)}$	50 and 65 Hz
−1, +3, −5, and +7	FADSC$_{4(1)}$ or FADSC$_{4(5)}$	25 and 50 Hz

E. Rotation Direction Correction for FADSC

DSC in the $\alpha\beta$ frame can be transformed from that in the dq frame by the Park transformation [27], which is based on the positive frequency. However, the conventional DSC fails to work with the negative frequency corresponding to the reverse rotation of the motor. This problem also existed in the FADSC, and it is solved by modifying $\boldsymbol{R}()$ given as

$$\boldsymbol{R_w}\ (\theta, \omega_e) = \begin{bmatrix} \cos\theta & -\text{sign}\left(\omega_e\right)\cdot\sin\theta \\ \text{sign}\left(\omega_e\right)\cdot\sin\theta & \cos\theta \end{bmatrix} \tag{21}$$

where sign() is the sign function.

Then, the expression of FADSC can be rewritten as

$$\begin{aligned} &\text{FADSC}_{n(m)}\ \left(\boldsymbol{e_s}\left[k_t\right], \omega_e\right) \\ &= \frac{1}{2}\,\boldsymbol{e_s}\left[k_t\right]\left(1 + \boldsymbol{R_w}\left(\frac{2\pi}{n}, \omega_e\right) z^{-D_m}\right). \end{aligned} \tag{22}$$

F. Implementation of FADSC

The proposed FADSC$_{n(m)}$ is still capable of eliminating harmonics given in (9). Nevertheless, a single FADSC cannot remove BEMF harmonics listed in Table I simultaneously whatever n is. Thus, a cascaded structure of multiple FADSCs similar to the cascaded DSC is necessary. The structure of the proposed FADSC is illustrated in Fig. 10, and it is applied after the LPF in SMO given in Fig. 2.

The main information of the cascaded FADSC for eliminating BEMF harmonics is given in Table II based on the above design principle.

IV. EXPERIMENTAL RESULTS

To verify the proposed FADSC, an experimental setup composed of a prototype IPMSM drive system is shown in Fig. 11. The control program is executed on the TMS320F28335, and the data are outputted to the oscilloscope by a D/A conversion circuit. The main parameters of the prototype IPMSM and control system are listed in Table III. The current offset error of phase A and the scaling error of phase B are set as 0.5A and +0.1 manually to simulate the serious current measurement errors. The cutoff frequencies of LPFs in the SMO and FADSC are both set as 100 Hz. The bandwidth of the PLL is set as 628.3 rad/s.

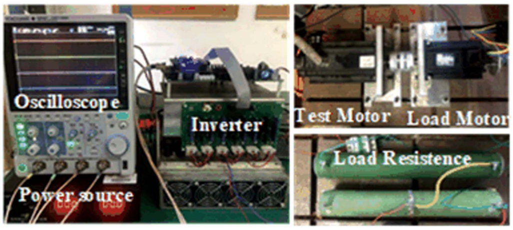

Fig. 11. Experimental equipment and platform of an IPMSM drive.

TABLE III
MAIN PARAMETERS OF THE IPMSM AND CONTROL SYSTEM

Description	Value	Description	Value
Rate voltage	200 V	Rated current	10 A
Rate speed	2000 r/min	Pole pairs	4
Record array length	60	Sampling frequency	10 Hz

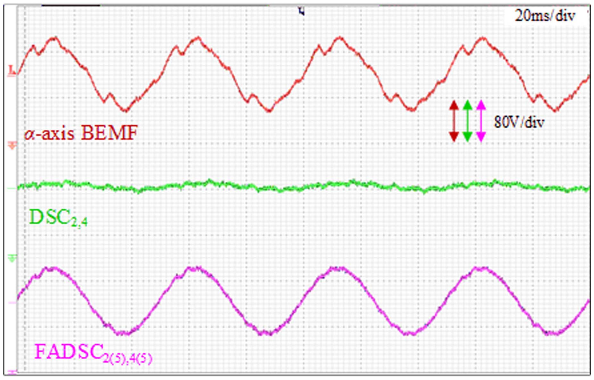

Fig. 12. Comparison of BEMF waveforms by different methods at −300 r/min (−20 Hz).

A. Effect of FADSC on BEMF Harmonic Elimination

Fig. 12 presents the α-axis BEMF estimated by SMO without extra filter (red), with DSC$_{2,4}$ (green) and with FADSC$_{2(5),4(5)}$ (purple) at −300 r/min (−20Hz). The subscripts of DSC and FADSC represent the cascaded types. Experimental results demonstrate that the conventional DSC fails to obtain a useful signal under reverse rotation, whereas the proposed FADSC can extract the fundamental component and suppress the harmonics.

In Fig. 13, the estimated α-axis BEMF processed by FADSC with different frequency-dividing recoding factors (FADSC$_{2(1),4(1)}$ and FADSC$_{2(5),4(5)}$) are tested and compared at 300 r/min (20 Hz) and 2000 r/min (133.3 Hz). Limited by the record array length and the approximation ability of the 2-order LI-FD, the phase and amplitude of α-axis BEMF filtered by FADSC$_{2(1),4(1)}$ are changed in a low-frequency state (20 Hz), as shown in Fig. 13(a). Fig. 13(b) reveals that the estimated α-axis BEMF is distorted by FADSC$_{2(5),4(5)}$ in a high-frequency state (133.3 Hz). These experimental results prove the correction of

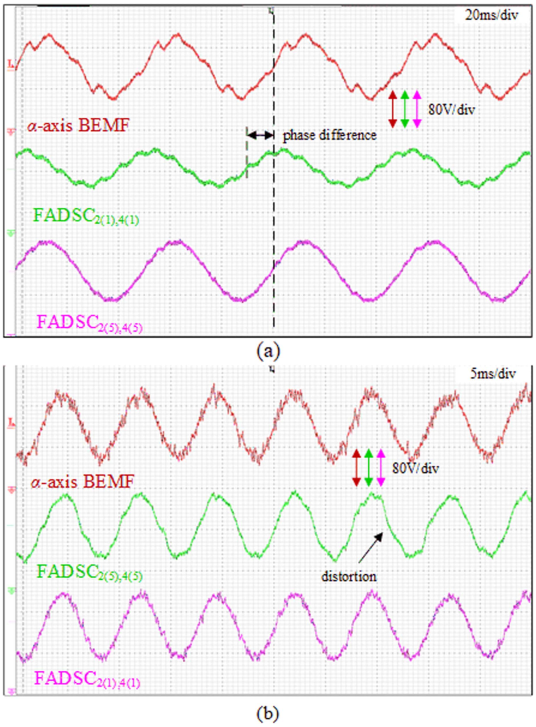

(a)

(b)

Fig. 13. Comparison of BEMF waveforms by different methods with FADSC$_{2(1),4(1)}$ and FADSC$_{2(5),4(5)}$. (a) 300 r/min (20 Hz). (b) 2000 r/min (133.33 Hz).

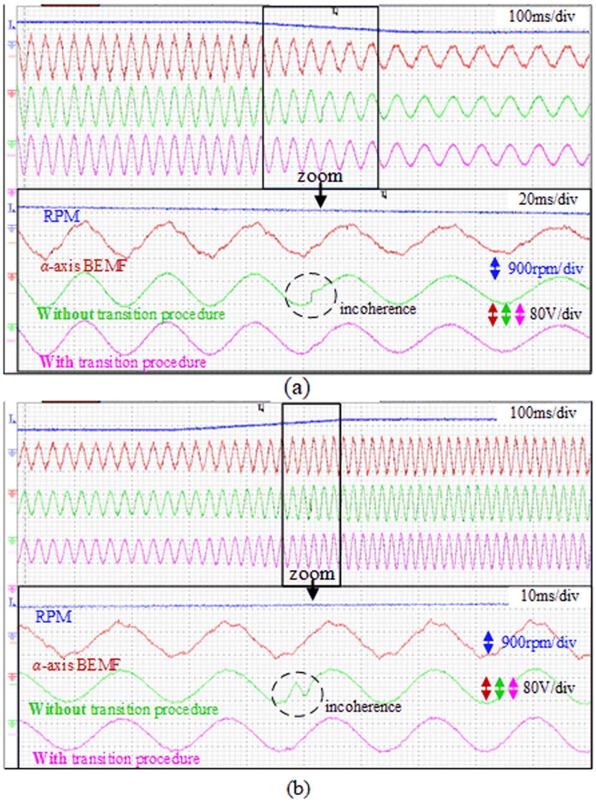

(a)

(b)

Fig. 14. Comparison of FADSC$_{n(m)}$ with/without transition procedure. (a) From 600 r/min (40 Hz) to 300 r/min (20 Hz). (b) From 600 r/min (40 Hz) to 900 r/min (60 Hz).

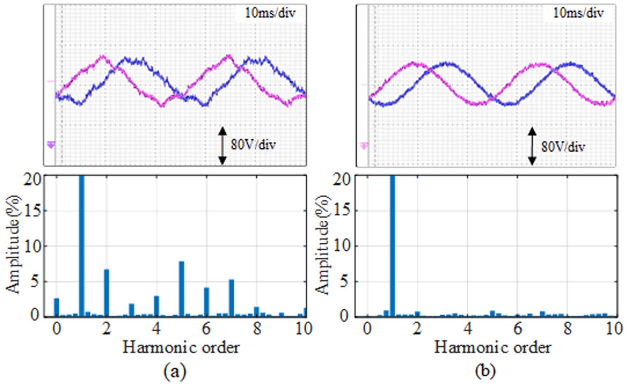

(a)

(b)

Fig. 15. Estimated $\alpha\beta$-axes BEMF and the spectrum of α-axis BEMF at 600 r/min. (a) Without the proposed FADSC. (b) With the proposed FADSC.

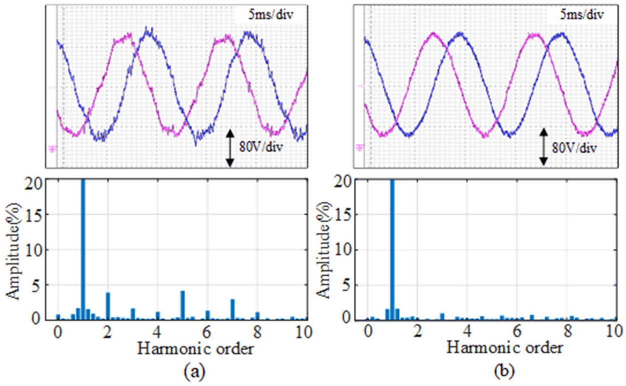

(a)

(b)

Fig. 16. Estimated $\alpha\beta$-axes BEMF and the spectrum of α-axis BEMF at 1500 r/min. (a) Without the proposed FADSC. (b) With the proposed FADSC.

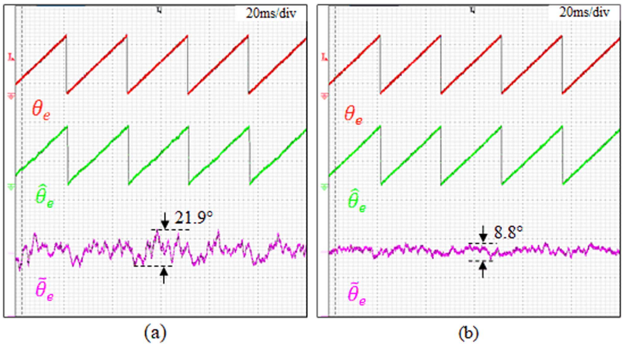

(a)

(b)

Fig. 17. Real and estimated rotor positions and the estimated position error at 600 r/min. (a) Without the proposed FADSC. (b) With the proposed FADSC.

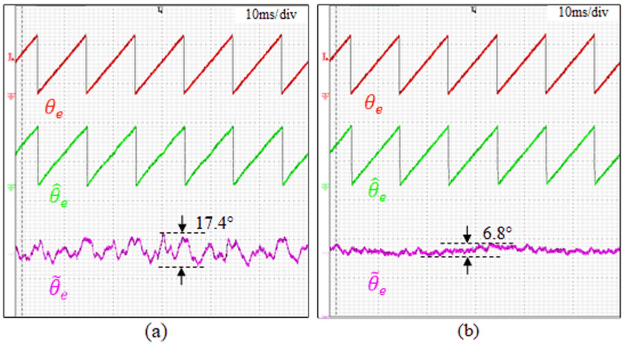

(a)

(b)

Fig. 18. Real and estimated rotor positions and the estimated position error at 1500 r/min. (a) Without the proposed FADSC. (b) With the proposed FADSC.

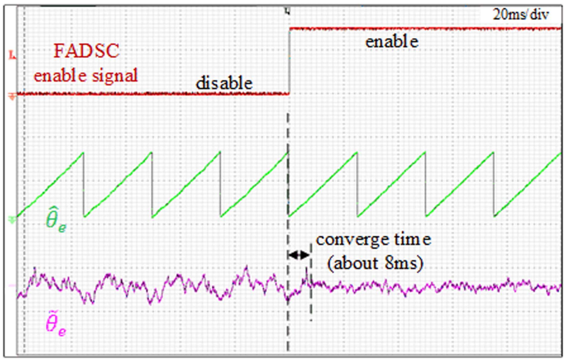

Fig. 19. Converge time of the proposed FADSC at 600 r/min.

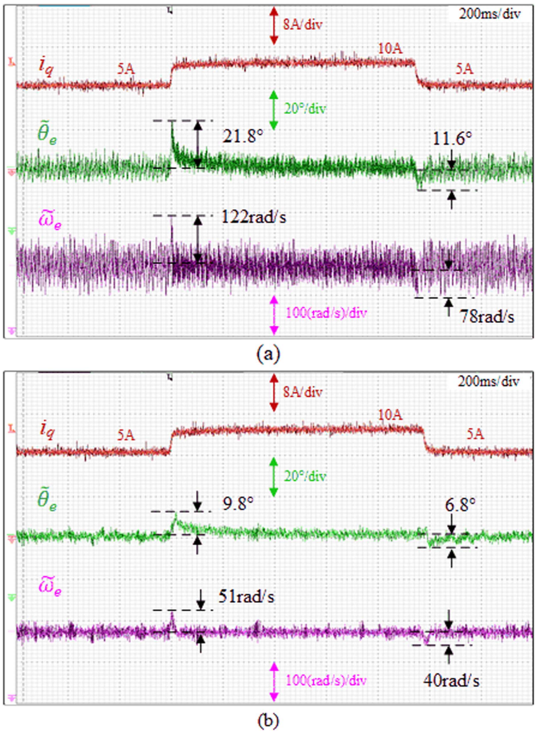

Fig. 20. Load changes from 50% to 100% and then to 50% at 900 r/min. (a) Without the proposed FADSC. (b) With the proposed FADSC.

the analysis of FADSC in Section III and the significance of the frequency-dividing record method is validated.

The necessity of the frequency-dividing factor changing procedure is verified in Fig. 14, where the estimated α-axis BEMF is distorted when the proposed changing procedure is not applied at the factor's changing moments.

B. Steady Experiments

The estimated BEMF and the spectrum of α-axis BEMF at 600 r/min and 1500 r/min are given in Figs. 15 and 16, respectively. The figures both illustrate that the estimated BEMF without the proposed FADSC have rich harmonics, e.g., 0, 2, 3, 5, and 7 orders, agreed well with the nonideal factors of the flux spatial harmonics, inverter nonlinearity, and current measurement errors. Also, even order harmonics exist in the estimated BEMF waveforms, but they have been eliminated thanks to FADSC$_2$. Figs. 15(b) and 16(b) show that the proposed FADSC can eliminate almost all the low-order harmonics effectively.

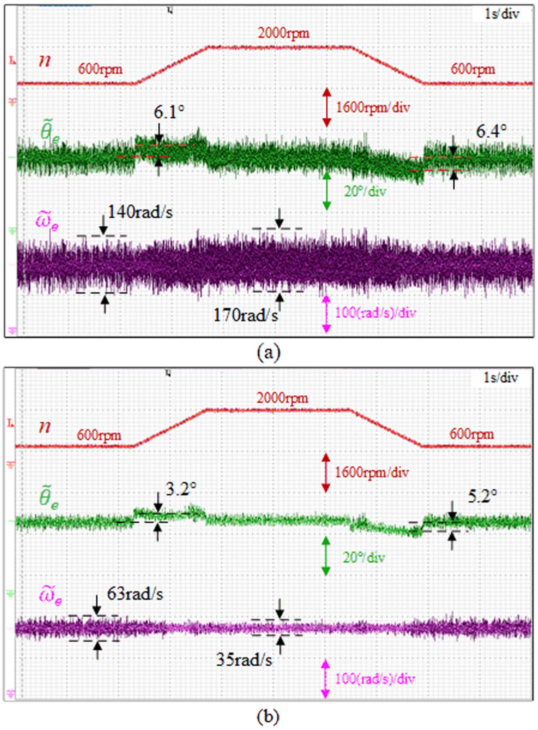

Fig. 21. Speed changes from 600 to 2000 r/min and then to 600 r/min. (a) Without the proposed FADSC. (b) With the proposed FADSC.

The estimated rotor positions with and without FADSC at 600 r/min are compared in Fig. 17. It can be seen that the proposed FADSC can suppress the fluctuations of the estimated rotor position error effectively. The same conclusion can also be obtained in the case of 1500 r/min as shown in Fig. 18.

The converging time of the proposed FADSC at 600 r/min is about 8 ms as shown in Fig. 19, which is about 1/4th of the fundamental period.

C. Transient Experiments

The transient experiments are divided into load-changing and speed-changing scenarios. As shown in Fig. 20, the load suddenly changes from 50% to 100% of the rated torque and then to 50% at a constant speed of 900 r/min. It is found that the proposed FADSC can suppress the fluctuations of the estimated position error and angular speed error effectively without affecting the dynamic performance of the drive system.

In Fig. 21, the speed first changes from 600 r/min to 2000 r/min and then back to 600 r/min again. As shown in Fig. 11, the load of the prototype IPMSM is a PMSM with the resistance load, which makes the phase currents' amplitudes large as the speed increases. Thus, the influence of the current measurement scaling error is large at high speed. This phenomenon is presented in Fig. 21(a). The influence of these unfavorable factors is suppressed thanks to the proposed FADSC. Consequently, the estimated position error and angular speed error are small, shown in Fig. 21(b).

V. CONCLUSION

This article aimed to eliminate the low-order harmonics caused by nonideal factors in BEMF estimated by SMO, and further reduce the rotor position estimation error in a sensorless IPMSM drive system. For this purpose, a filter based on FADSC extended from the conventional DSC was proposed to eliminate multiple harmonics simultaneously with a simple structure.

The following modifications were adopted to realize FADSC.

1) The Lagrange interpolation was adopted to realize FD.
2) The frequency-dividing record method was proposed to overcome the limitation of record array length at low speed.
3) The changing procedure for switching different frequency-dividing factors was proposed.
4) A new transformation matrix was designed to suit both the both forward and reverse rotations.

Besides, the principles for designing the main parameters of the proposed FADSC were given in detail. Its effectiveness was demonstrated by experimental results. As a result, the accuracy of estimated rotor position in an SMO-based sensorless drive system was improved even considering serious nonideal factors.

REFERENCES

[1] X. Li, Z. Xue, X. Yan, L. Zhang, W. Ma, and W. Hua, “Low-complexity multivector-based model predictive torque control for PMSM with voltage preselection,” *IEEE Trans. Power Electron.*, vol. 36, no. 10, pp. 11726–11738, Oct. 2021.

[2] J. Lara, J. Xu, and A. Chandra, “A novel algorithm based on polynomial approximations for an efficient error compensation of magnetic analog encoders in PMSMs for EVs,” *IEEE Trans. Ind. Electron.*, vol. 63, no. 6, pp. 3377–3388, Jun. 2016.

[3] S. Chen, Y. Zhao, H. Qiu, and X. Ren, “High-precision rotor position correction strategy for high-speed permanent magnet synchronous motor based on resolver,” *IEEE Trans. Power Electron.*, vol. 35, no. 9, pp. 9716–9726, Sep. 2020.

[4] Y. Wang, K. Liu, W. Hua, C. Zhang, Z. Wu, and H. Zhang, “Analysis and detection of rotor eccentricity in permanent magnet synchronous machines based on linear Hall sensors,” *IEEE Trans. Power Electron.*, vol. 37, no. 4, pp. 4719–4729, Apr. 2022.

[5] A. Varatharajan, G. Pellegrino, E. Armando, and M. Hinkkanen, “Sensorless synchronous motor drives: A review of flux observer-based position estimation schemes using the projection vector framework,” *IEEE Trans. Power Electron.*, vol. 36, no. 7, pp. 8171–8180, Jul. 2021.

[6] G. Wang, M. Valla, and J. Solsona, “Position sensorless permanent magnet synchronous machine drives—A review,” *IEEE Trans. Ind. Electron.*, vol. 67, no. 7, pp. 5830–5842, Jul. 2020.

[7] Z. Yin, Y. Zhang, X. Cao, D. Yuan, and J. Liu, “Estimated position error suppression using novel PLL for IPMSM sensorless drives based on full-order SMO,” *IEEE Trans. Power Electron.*, vol. 37, no. 4, pp. 4463–4474, Apr. 2022.

[8] R. Cao, N. Jiang, and M. Lu, “Sensorless control of linear flux-switching permanent magnet motor based on extended Kalman filter,” *IEEE Trans. Ind. Electron.*, vol. 67, no. 7, pp. 5971–5979, Jul. 2020.

[9] M. Hinkkanen, S. E. Saarakkala, H. A. A. Awan, E. Mölsä, and T. Tuovinen, “Observers for sensorless synchronous motor drives: Framework for design and analysis,” *IEEE Trans. Ind. Appl.*, vol. 54, no. 6, pp. 6090–6100, Nov. 2018.

[10] A. Apte, V. A. Joshi, H. Mehta, and R. Walambe, “Disturbance-observer-based sensorless control of PMSM using integral state feedback controller,” *IEEE Trans. Power Electron.*, vol. 35, no. 6, pp. 6082–6090, Jun. 2020.

[11] K. K. Prabhakaran and A. Karthikeyan, “Electromagnetic torque-based model reference adaptive system speed estimator for sensorless surface mount permanent magnet synchronous motor drive,” *IEEE Trans. Ind. Electron.*, vol. 67, no. 7, pp. 5936–5947, Jul. 2020.

[12] B. Wang, Y. Shao, Y. Yu, Q. Dong, Z. Yun, and D. Xu, “High-order terminal sliding-mode observer for chattering suppression and finite-time convergence in sensorless SPMSM drives,” *IEEE Trans. Power Electron.*, vol. 36, no. 10, pp. 11910–11920, Oct. 2021.

[13] K. Zhang, M. Fan, Y. Yang, Z. Zhu, C. Garcia, and J. Rodriguez, “An improved adaptive selected harmonic elimination algorithm for current measurement error correction of PMSMs,” *IEEE Trans. Power Electron.*, vol. 36, no. 11, pp. 13128–13138, Nov. 2021.

[14] S. Ye and X. Yao, “An enhanced SMO-based permanent-magnet synchronous machine sensorless drive scheme with current measurement error compensation,” *IEEE J. Emerg. Sel. Top. Power Electron.*, vol. 9, no. 4, pp. 4407–4419, Aug. 2021.

[15] J. Han, B.-H. Kim, and S. K. Sul, “Effect of current measurement error in angle estimation of permanent magnet AC motor sensorless control,” in *Proc. IEEE 3rd Int. Future Energy Electron. Conf. ECCE Asia*, 2017, pp. 2171–2176.

[16] Y. Zhao, W. Qiao, and L. Wu, “Dead-time effect analysis and compensation for a sliding-mode position observer-based sensorless IPMSM control system,” *IEEE Trans. Ind. Appl.*, vol. 51, no. 3, pp. 2528–2535, May 2015.

[17] D. Liang, J. Li, R. Qu, and W. Kong, “Adaptive second-order sliding-mode observer for PMSM sensorless control considering VSI nonlinearity,” *IEEE Trans. Power Electron.*, vol. 33, no. 10, pp. 8994–9004, Oct. 2018.

[18] Y. Wang, Y. Xu, and J. Zou, “Sliding-mode sensorless control of PMSM with inverter nonlinearity compensation,” *IEEE Trans. Power Electron.*, vol. 34, no. 10, pp. 10206–10220, Oct. 2019.

[19] X. Song, J. Fang, B. Han, and S. Zheng, “Adaptive compensation method for high-speed surface PMSM sensorless drives of EMF-based position estimation error,” *IEEE Trans. Power Electron.*, vol. 31, no. 2, pp. 1438–1449, Feb. 2016.

[20] D. Bao, X. Pan, Y. Wang, X. Wang, and K. Li, “Adaptive synchronous-frequency tracking-mode observer for the sensorless control of a surface PMSM,” *IEEE Trans. Ind. Appl.*, vol. 54, no. 6, pp. 6460–6471, Nov. 2018.

[21] Q. An, J. Zhang, Q. An, X. Liu, A. Shamekov, and K. Bi, “Frequency-adaptive complex-coefficient filter-based enhanced sliding mode observer for sensorless control of permanent magnet synchronous motor drives,” *IEEE Trans. Ind. Appl.*, vol. 56, no. 1, pp. 335–343, Jan. 2020.

[22] G. Wang, H. Zhan, G. Zhang, X. Gui, and D. Xu, “Adaptive compensation method of position estimation harmonic error for EMF-based observer in sensorless IPMSM drives,” *IEEE Trans. Power Electron.*, vol. 29, no. 6, pp. 3055–3064, Jun. 2014.

[23] G. Wang, T. Li, G. Zhang, X. Gui, and D. Xu, “Position estimation error reduction using recursive-least-square adaptive filter for model-based sensorless interior permanent-magnet synchronous motor drives,” *IEEE Trans. Ind. Electron.*, vol. 61, no. 9, pp. 5115–5125, Sep. 2014.

[24] X. Wu et al., “Enhanced position sensorless control using bilinear recursive least squares adaptive filter for interior permanent magnet synchronous motor,” *IEEE Trans. Power Electron.*, vol. 35, no. 1, pp. 681–698, Jan. 2020.

[25] G. Zhang, G. Wang, D. Xu, and N. Zhao, “ADALINE-network-based PLL for position sensorless interior permanent magnet synchronous motor drives,” *IEEE Trans. Power Electron.*, vol. 31, no. 2, pp. 1450–1460, Feb. 2016.

[26] S. Gude and C.-C. Chu, “Three-phase PLLs by using frequency adaptive multiple delayed signal cancellation prefilters under adverse grid conditions,” *IEEE Trans. Ind. Appl.*, vol. 54, no. 4, pp. 3832–3844, Jul. 2018.

[27] Y. F. Wang and Y. W. Li, “Three-phase cascaded delayed signal cancellation PLL for fast selective harmonic detection,” *IEEE Trans. Ind. Electron.*, vol. 60, no. 4, pp. 1452–1463, Apr. 2013.

[28] T. I. Laakso, V. Valimaki, M. Karjalainen, and U. K. Laine, “Splitting the unit delay [FIR/all pass filters design],” *IEEE Signal Process. Mag.*, vol. 13, no. 1, pp. 30–60, Jan. 1996.

Zheng Wu received the B.Sc. degree in electrical engineering from the School of Electrical Engineering, Southeast University, Nanjing, China, in 2018 , where he is currently working toward the Ph.D. degree in electrical engineering.

His research interests include sensorless control technology, multiphase motor, and fault-tolerance strategy.

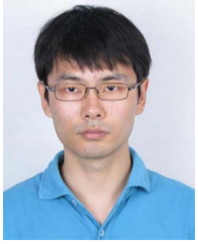

Chenwen Cheng received the B.S. and Ph.D. degrees from Zhejiang University, Hangzhou, China, in 2012 and 2017, respectively, both in electrical engineering.

From 2018 to 2021, he was a postdoc researcher with San Diego State University, San Diego, CA, USA. He is currently with Southeast University. His research interests include motor control, renewable power generation, and wireless power transfer technologies.

Wei Hua (Senior Member, IEEE) received the B.Sc. and Ph.D. degrees in electrical engineering from Southeast University, Nanjing, China, in 2001 and 2007, respectively.

From 2004 to 2005, he was a joint-supervised Ph.D. student with the Department of Electronics and Electrical Engineering, The University of Sheffield, Sheffield, U.K. Since 2007, he has been with Southeast University, where he is currently a Chief Professor and a Distinguished Professor of Jiangsu Province. He has co-authored more than 150 technical papers. He holds 50 patents in his areas of interest.

His teaching and research interests include the design, analysis, and control of electrical machines, especially for permanent magnet brushless machines and switching reluctance machines.

Yuchen Wang was born in Shanxi, China, in 1994. He received the B.Sc. degree in electrical engineering in 2017 from the School of Electrical Engineering, Southeast University, Nanjing, China, where he is currently working toward the Ph.D. degree in electrical engineering.

His current research interests include the analysis and design of embedded magnetic encoders.

Hengliang Zhang was born in Anhui, China, in 1992. He received the B.Sc. and Ph.D. degrees in electrical engineering from Southeast University, Nanjing, China, in 2014 and 2020, respectively.

From 2018 to 2019, he was a joint-supervised Ph.D. student with the Power Electronics, Machines and Control Group, University of Nottingham, Nottingham, U.K. He is currently a Lecturer with Southeast University. His research interests include the design and analysis of permanent magnet machines in electric vehicles and servo systems.

Wei Wang (Senior Member, IEEE) was born in Jiangsu, China. He received the B.Sc. degree in electrical engineering from Nanjing University of Science and Technology, Nanjing, China, in 2008, and the Ph.D. degree in electrical engineering from Southeast University, Nanjing in 2014.

Since 2014, he has been with Southeast University, where he is currently an Associate Professor in the School of Electrical Engineering. From October 2011 to October 2012, he was the recipient of the scholarship from China Scholarship Council and was a joint Ph.D. student with the University of Lille 1, Lille, France. He is the author or coauthor of more than 30 technical papers. His research interests include motor drives and traction systems for rail transit.